ФИЗИКА ЭЛЕМЕНТАРНЫХ ЧАСТИЦ И АТОМНОГО ЯДРА
2003. Т. 34. ВЫП. 4

УДК 539.17.17

LIGHT FRONT VARIABLES IN HIGH-ENERGY HADRON–HADRON AND NUCLEUS–NUCLEUS INTERACTIONS

L. Chkhaidze, T. Djobava[*]*, Yu. Tevzadze*

High Energy Physics Institute, Tbilisi State University, Tbilisi, Georgia

V. Garsevanishvili

Mathematical Institute of the Georgian Academy of Sciences, Tbilisi, Georgia

[*]e-mail: djobava@sun20.hepi.edu.ge

ФИЗИКА ЭЛЕМЕНТАРНЫХ ЧАСТИЦ И АТОМНОГО ЯДРА
2003. Т. 34. ВЫП. 4

УДК 539.17.17

LIGHT FRONT VARIABLES IN HIGH-ENERGY HADRON–HADRON AND NUCLEUS–NUCLEUS INTERACTIONS

L. Chkhaidze, T. Djobava[*], *Yu. Tevzadze*

High Energy Physics Institute, Tbilisi State University, Tbilisi, Georgia

V. Garsevanishvili

Mathematical Institute of the Georgian Academy of Sciences, Tbilisi, Georgia

Light front variables are introduced to study inclusive spectra of secondaries in hadron–hadron and nucleus–nucleus interactions. It is established that the phase space of secondary pions is divided into two parts with significantly different characteristics. The thermal equilibrium seems to be reached in one of these parts. Corresponding temperatures of pions in hadron–hadron and nucleus–nucleus collisions are extracted. The results are compared with the results of other types of analysis. The results for nucleus–nucleus collisions are compared with the predictions of the Quark-Gluon String Model (QGSM). The QGSM satisfactorily reproduces the experimental data for light and intermediate-mass nuclei.

Введены переменные светового фронта для изучения инклюзивных спектров вторичных частиц в адрон-адронных и ядро-ядерных соударениях. Фазовое пространство вторичных пионов естественным образом разбивается на две части с существенно различными характеристиками. Представляется правдоподобным, что в одной из этих частей достигается тепловое равновесие. Извлечены соответствующие температуры пионов в адрон-адронных и ядро-ядерных соударениях. Результаты сравниваются с результатами анализов другого типа. Результаты для ядро-ядерных соударений сравниваются с предсказаниями кварк-глюонной модели струн (КГМС). КГМС удовлетворительно воспроизводит экспериментальные данные для легких и средних ядер.

1. INTRODUCTION. DEFINITION AND PROPERTIES OF VARIABLES

The study of single-particle inclusive processes [1] remains one of the simplest and effective tools for the investigation of multiple production of secondaries at high energies. The consequences of the limiting fragmentation hypothesis [2] and those of the parton model [3] and the principle of automodelity for strong interactions [4] have been formulated in this way.

At high energies different dynamical mechanisms contribute to spectra of secondaries. Among them «pionization» and fragmentation mechanisms are widely

[*]e-mail: djobava@sun20.hepi.edu.ge

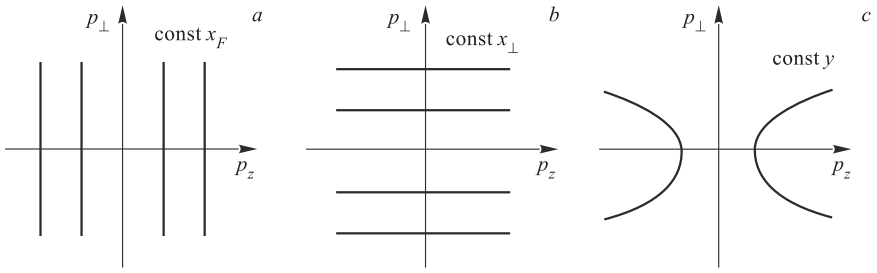

Fig. 1. The schematic view of the surfaces of constants x_F (*a*), $x_\perp$ (*b*), and y (*c*) in the $(p_z, p_\perp)$ plane

discussed. «Pionization» means the existence of secondary pions with relatively low momenta and flat (almost isotropic) angular distribution in the centre-of-mass frame of colliding objects. The fragmentation component has sharply anisotropic angular distribution in the centre-of-mass frame. One of the principal problems in this direction is the separation of these two components. Up to now, there exist no unique way to separate these mechanisms. Different authors propose different ways and non of them seems to be satisfactory. It will be shown that the presentation of inclusive spectra in terms of light front variables provides a unique possibility of separating these two components.

An important role in establishing many properties of multiple production is played by the choice of kinematic variables in terms of which observable quantities are presented (see, e. g., [5–7]). The variables which are commonly used are the following: the Feynman $x_F = 2p_z/\sqrt{s}$, rapidity $y = 1/2 \ln[(E + p_z)/(E - p_z)]$, transverse scaling variable $x_T = 2p_T/\sqrt{s}$, etc. In the case of azimuthal symmetry, the surfaces of constant x_F are the planes $p_z = x_F\sqrt{s}/2$, the surfaces of constant y are the hyperboloids

$$p_z^2\left[\left(\frac{1+e^{2y}}{1-e^{2y}}\right)^2 - 1\right] - p_T^2 = m^2,$$

and the surfaces of constant x_T are the planes $p_T = x_T\sqrt{s}/2$ in the phase space (see Fig. 1).

Unified scale invariant variables for the presentation of single-particle inclusive distributions have been proposed [8], the properties of which are described below.

Consider an arbitrary 4-momentum $p_\mu(p_0, \mathbf{p})$ and introduce light front combinations [9]:

$$p_\pm = p_0 \pm p_3. \tag{1}$$

If the 4-momentum p_μ is on the mass shell ($p^2 = m^2$), the combinations $p_\pm, \mathbf{p}_T$ (where $\mathbf{p}_T = (p_1, p_2)$) define the so-called horospherical coordinate system (see, e. g., [10, 11]) on the corresponding mass-shell hyperboloid $p_0^2 - \mathbf{p}^2 = m^2$ ($u = p/m$, $u_0^2 - \mathbf{u}^2 = 1$). Corresponding hyperboloid in the velocity space is the realization of the curved space with constant negative curvature, i. e., the Lobachevsky space.

The following relations define the horospherical coordinate system:

$$u_0 + u_3 = e^a, \tag{2}$$

$$u_0 - u_3 = e^{-a} + e^a \boldsymbol{\gamma}_\perp^2, \tag{3}$$

$$\mathbf{u}_\perp = (u_1, u_2) = e^a \boldsymbol{\gamma}_\perp, \tag{4}$$

where $\boldsymbol{\gamma}_\perp = (\gamma_1, \gamma_2)$

$$(u_1, u_2, u_3) \to (e^a, \boldsymbol{\gamma}_\perp), \tag{5}$$

$$\frac{d\mathbf{p}}{E} = e^{2a} da d\boldsymbol{\gamma}_\perp, \tag{6}$$

$$E\frac{d\sigma}{d\mathbf{p}} = \frac{1}{\pi m^2}\frac{d\sigma}{da d\boldsymbol{\gamma}_\perp^2}. \tag{7}$$

In particular, if $a = 0$, $u_0 + u_3 = 1$. Thus the horosphere in the Lobachevsky space, realized on the upper sheet of the hyperboloid $u_0^2 - \mathbf{u}^2 = 1$, is a two-dimensional surface with Euclidean intrinsic geometry. Coordinates $(a, \boldsymbol{\gamma}_\perp)$ are related to measurable quantities $(p_z, \mathbf{p}_\perp)$ as follows:

$$a = \ln \frac{E + p_z}{m} = \ln \frac{\sqrt{\mathbf{p}_\perp^2 + p_z^2 + m^2} + p_z}{m}, \tag{8}$$

$$\boldsymbol{\gamma}_\perp = \frac{\mathbf{p}_\perp}{E + p_z} = \frac{\mathbf{p}_\perp}{\sqrt{\mathbf{p}_\perp^2 + p_z^2 + m^2} + p_z}, \quad \mathbf{p}_\perp = \mathbf{p}_T. \tag{9}$$

Let us construct scale invariant variables:

$$\xi^\pm = \pm\frac{p_\pm^c}{p_\pm^a + p_\pm^b} \tag{10}$$

in terms of the 4-momenta $p_\mu^a,\ p_\mu^b,\ p_\mu^c$ of particles $a,\ b,\ c$, entering the inclusive reaction $a + b \to c + X$. The z axis is taken to be the collision axis, i. e., $p_z = p_3$. Particles a and b can be hadrons, heavy ions, leptons.

It is interesting to note the properties of $\xi^\pm$ variables in some limiting cases. The light front variables $\xi^\pm$ in the centre-of-mass frame are defined as follows [8]:

$$\xi^\pm = \pm\frac{E \pm p_z}{\sqrt{s}} = \pm\frac{E + |p_z|}{\sqrt{s}}, \tag{11}$$

where s is the usual Mandelstam variable; $E = \sqrt{p_z^2 + p_T^2 + m^2}$ and p_z are the energy and the z component of the momentum of produced particle. The upper sign in Eq. (11) is used for the right-hand side hemisphere; and the lower sign, for the left-hand side hemisphere.

In order to enlarge the scale in the region of small $\xi^{\pm}$, it is convenient also to introduce the variables

$$\zeta^{\pm} = \mp \ln |\xi^{\pm}|. \tag{12}$$

The ζ^{+} variable is related to a via the following relation:

$$\zeta^{+} = -a - \ln \frac{m}{\sqrt{s}}.$$

The invariant differential cross section in terms of these variables looks as follows:

$$E\frac{d\sigma}{d\mathbf{p}} = \frac{|\xi^{\pm}|}{\pi} \frac{d\sigma}{d\xi^{\pm} dp_T^2} = \frac{1}{\pi} \frac{d\sigma}{d\zeta^{\pm} dp_T^2}. \tag{13}$$

In the limits of high p_z ($|p_z| \gg p_T$) and high p_T ($p_T \gg |p_z|$), the $\xi^{\pm}$ variables go over to the well-known variables

$$\xi^{\pm} \to \frac{2p_z}{\sqrt{s}} = x_F, \quad \xi^{\pm} \to \frac{m_T}{\sqrt{s}} \to \frac{p_T}{\sqrt{s}} = \frac{x_T}{2}, \quad m_T = \sqrt{p_T^2 + m^2},$$

respectively, which are intensively used in high-energy physics. $\xi^{\pm}$ variables are related to x_F, x_T and rapidity y as follows:

$$\xi^{\pm} = \frac{1}{2}\left(x_F \pm \sqrt{x_F^2 + x_T^2}\right), \quad x_T = \frac{2m_T}{\sqrt{s}}, \tag{14}$$

$$y = \pm\frac{1}{2} \ln \frac{(\xi^{\pm}\sqrt{s})^2}{m_T^2}. \tag{15}$$

The region $|\xi^{\pm}| < m/\sqrt{s}$ is kinematically forbidden for the $\xi^{\pm}$ spectra integrated over all values of p_T^2, and the region $|\xi^{\pm}| < m_T/\sqrt{s}$ is forbidden for the $\xi^{\pm}$ spectra at fixed values of p_T^2. The minimum value of $\xi^{\pm} = \pm m/\sqrt{s}$ we call the threshold value.

Light front variables have been introduced by Dirac [9], and they are widely used now in theoretical studies of relativistic composite systems (see, e. g., [12–26], in theoretical and experimental studies of nuclear reactions with beams of relativistic nuclei (see, e. g., [22, 27, 28]) and in the study of quark confinement in QCD (see, e. g., [29]). Combinations like Eq. (1) appear also when considering the scale transformations [30] in the theory with fundamental length (see, e. g., [31]).

2. INCLUSIVE DISTRIBUTIONS IN HADRON–HADRON COLLISIONS

Using $\xi^{\pm}$ variables, inclusive reactions in $\pi^- p$ interactions at 5 and 40 GeV/c have been analysed. The following reactions have been studied:

$$\pi^- p \to \pi^+ + X, \tag{16}$$

$$\pi^- p \to \pi^- + X, \tag{17}$$

$$\pi^- p \to \gamma + X, \tag{18}$$

$$\pi^- p \to K^0 + X, \tag{19}$$

$$\pi^- p \to \Lambda^0 + X; \tag{20}$$

and the following experimental data have been used: for the reaction (16) we have 19500 inelastic events detected in the one-metre Hydrogen Bubble Chamber of JINR [32]; for the reactions (17) and (18) at 5 GeV/c we have 7900 events detected in the one-metre Propane Bubble Chamber of JINR [33]; for the reactions (16)–(20) at 40 GeV/c we have 14300 inelastic events in the two-metre Propane Bubble Chamber of JINR [34].

Experimental data for π^- mesons obtained at both energies are presented in the form of invariant differential cross sections $\dfrac{|\xi^{\pm}|}{\pi}\dfrac{d\sigma}{d\xi^{\pm}}$ and $\dfrac{|\xi^{\pm}|}{\pi}\dfrac{d\sigma}{d\xi^{\pm} dp_T^2}$ in

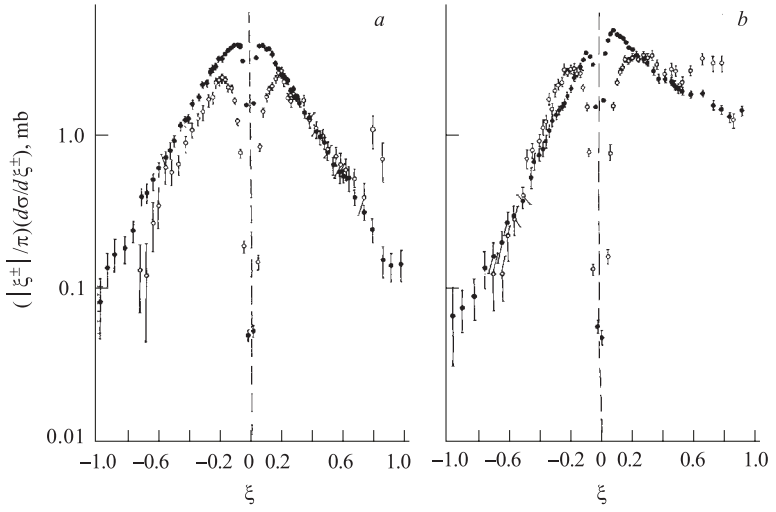

Fig. 2. The $\xi^{\pm}$ distribution of π^+ (*a*) and π^- mesons (*b*) from $\pi^- p$ collisions at 5 (○) and 40 GeV/c (●) of incident momentum

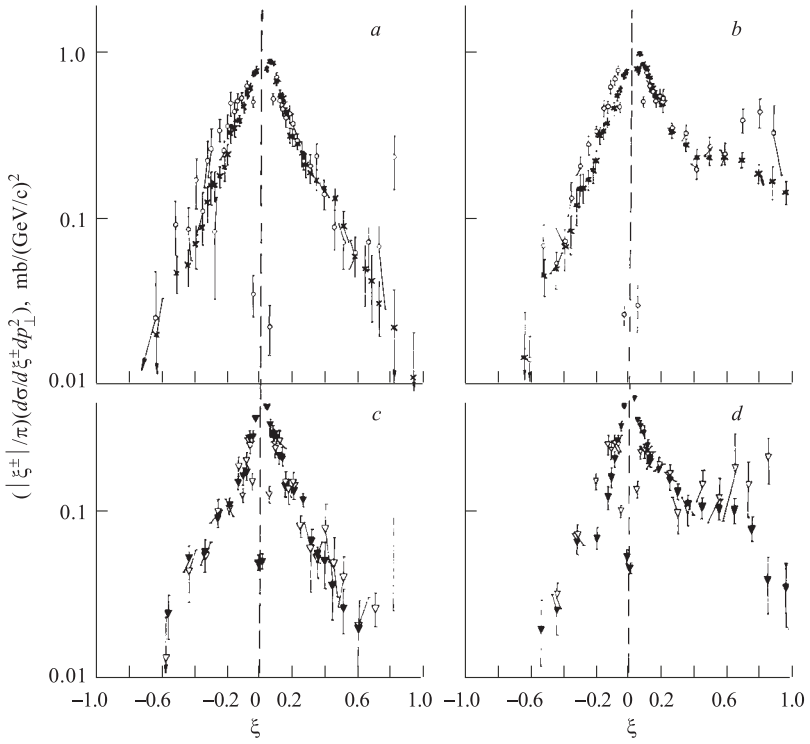

Fig. 3. The $\xi^{\pm}$ distribution of π^+ (a, c) and π^- mesons (b, d) from $\pi^- p$ collisions at different intervals of transverse momentum: $a, b)$ $0.1 < p_{\perp} < 0.2$ GeV/c: $\circ$ — 5 GeV/c; $\times$ — 40 GeV/c of incident momentum; $c, d)$ $0.0 < p_{\perp} < 0.1$ GeV/c: $\triangledown$ — 5 GeV/c; $\blacktriangledown$ — 40 GeV/c of incident momentum

Figs. 2–5. For comparison, in Fig. 6, the data for the reaction (16) at the same energies are given as function of the usual Feynman variable x_F.

$\xi^{\pm}$ distributions have two features, which make them differ from corresponding x_F distributions: 1) Existence of the forbidden region near the point $\xi^{\pm} = 0$ (cross sections vanish in the region $|\xi^{\pm}| \leq m^c/\sqrt{s}$). Corresponding threshold values $\xi^{\pm}_{\rm th}$ for various types of particles in various $p_{\perp}$ intervals are given in Tables 1 and 2; 2) Existence of maxima at some $\tilde{\xi^{\pm}}$ in the region of relatively small $|\xi^{\pm}|$. Maxima in $\xi^{\pm}$ distributions become less pronounced with increasing mass of the detected particle. For γ quanta and π mesons we have well pronounced peaks in the region of small $|\xi^{\pm}|$, for K^0 mesons, and especially for Λ^0 hyperons, we have more smooth behaviour.

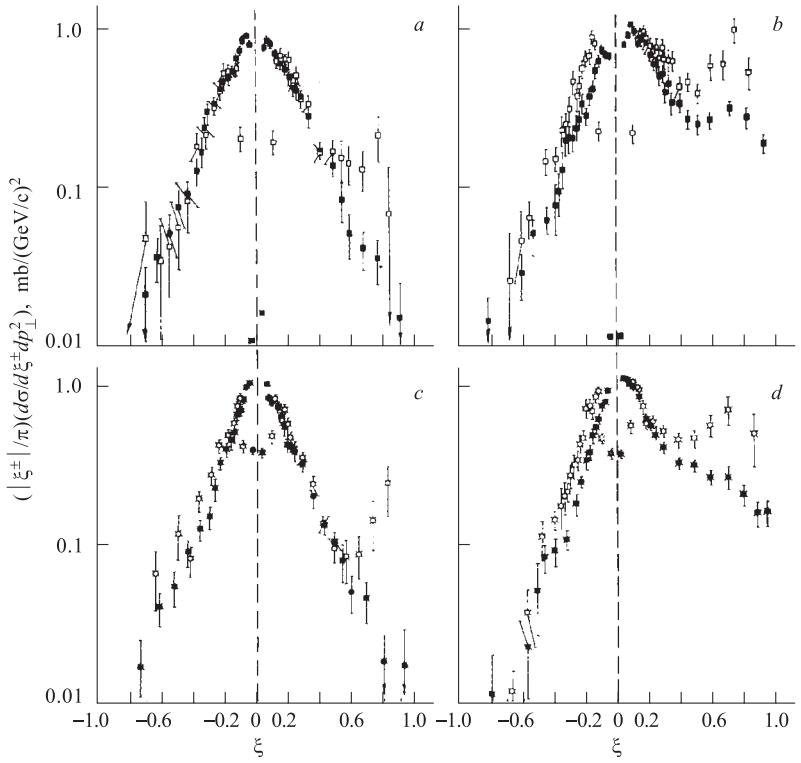

Fig. 4. The $\xi^{\pm}$ distribution of π^+ (a, c) and π^- mesons (b, d) from $\pi^- p$ collisions at different intervals of transverse momentum: $a, b)$ $0.3 < p_{\perp} < 0.4$ GeV/c: □ — 5 GeV/c; ■ — 40 GeV/c of incident momentum; $c, d)$ $0.2 < p_{\perp} < 0.3$ GeV/c: ○ — 5 GeV/c; • — 40 GeV/c of incident momentum

Differential cross sections as functions of $\xi^{\pm}$ variables at 5 and 40 GeV/c in the region $|\xi^{\pm}| > |\tilde{\xi}^{\pm}|$ are rather close to each other. This allows one to speak about the approximate scale invariance (automodelity) in some regions of phase space.

In order to study the nature of these maxima, we have investigated the angular and $p_{\perp}^2$ distributions of $\pi^{\pm}$ mesons in $\pi^- p$ interactions at 40 GeV/c in the regions $|\xi^{\pm}| < |\tilde{\xi}^{\pm}|$ and $|\xi^{\pm}| > |\tilde{\xi}^{\pm}|$ separately [35]. Results for π^+ mesons are presented in Fig. 7. The angular distribution of particles with $|\xi^{\pm}| > |\tilde{\xi}^{\pm}|$ is sharply anisotropic in contrast to the almost flat distribution of particles with $|\xi^{\pm}| < |\tilde{\xi}^{\pm}|$. The slopes of $p_{\perp}^2$ distributions differ substantially.

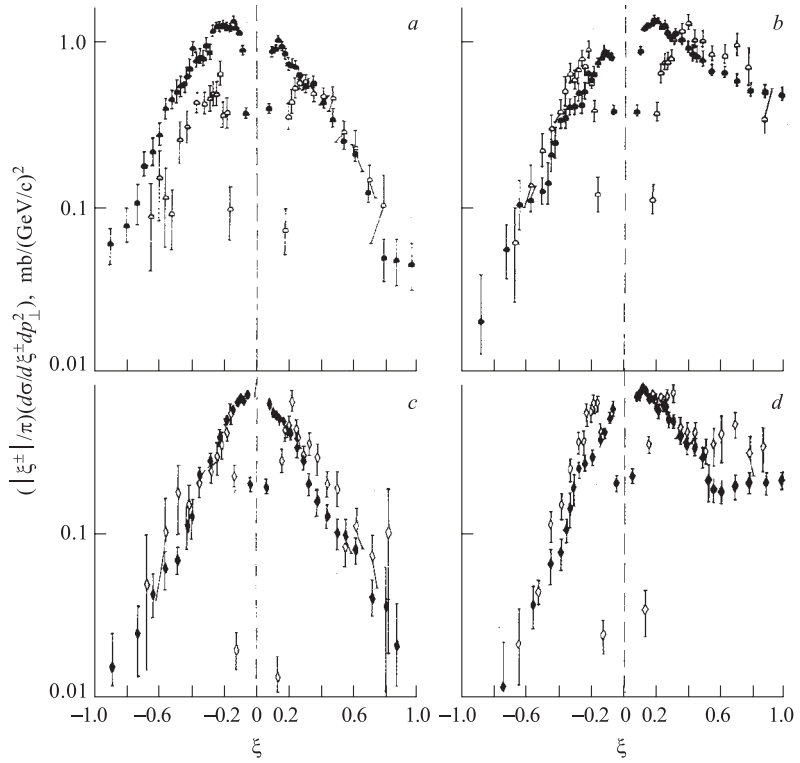

Fig. 5. The $\xi^{\pm}$ distribution of π^+ (a, c) and π^- mesons (b, d) from $\pi^- p$ collisions at different intervals of transverse momentum: $a, b)$ $0.5 < p_{\perp} < 1.0$ GeV/c: ○ — 5 GeV/c; • — 40 GeV/c of incident momentum; $c, d)$ $0.4 < p_{\perp} < 0.5$ GeV/c: ◇ — 5 GeV/c; ◆ — 40 GeV/c of incident momentum

Note, that the surfaces of constant $\xi^{\pm}$ are the paraboloids

$$p_z^c = \frac{p_{\perp}^{c^2} + m^{c^2} - (\xi^{\pm}\sqrt{s})^2}{-2\xi^{\pm}\sqrt{s}} \tag{21}$$

Table 1. **Threshold values and the values corresponding to the points of maxima $(\tilde{\xi}^+, \tilde{\xi}^-)$ of $\xi^{\pm}$ variables for inclusive spectra**

Particle type	5 GeV/c			40 GeV/c		
	$\lvert\xi_{\rm th}^{\pm}\rvert = m^c/\sqrt{s}$	$\tilde{\xi}^+$	$\tilde{\xi}^-$	$\lvert\xi_{\rm th}^{\pm}\rvert = m^c/\sqrt{s}$	$\tilde{\xi}^+$	$\tilde{\xi}^-$
γ	0	0.080	–0.120	0	0.040	–0.040
π^+	0.040	0.190	–0.190	0.016	0.070	–0.090
π^-	0.040	0.170	–0.170	0.016	0.090	–0.090
K^0	0.150	0.325	–0.275	0.060	0.150	–0.150
Λ^0	0.350	0.500	–0.550	0.130		–0.550

in the phase space (Fig. 8). Thus the paraboloids

$$p_z^c = \frac{p_\perp^{c^2} + m^{c^2} - (\tilde{\xi}^+\sqrt{s})^2}{-2\tilde{\xi}^+\sqrt{s}} \quad (22)$$

separate two groups of particles with significantly different characteristics.

Further analysis of inclusive reactions in terms of light front variables has been performed by means of $\zeta^\pm$ variables (see Eq. (12)). Experimental data for invariant differential cross sections $1/\pi\, d\sigma/d\zeta^\pm$ in the reaction (16) at 5 and 40 GeV/c are presented in Fig. 9. Maxima at $\tilde{\zeta}^\pm$ are also observed. However, the region $|\xi^\pm| < |\tilde{\xi}^\pm|$ goes over to the region $|\zeta^\pm| > |\tilde{\zeta}^\pm|$ and vice versa (see Eqs. (11) and (12)). It is in-

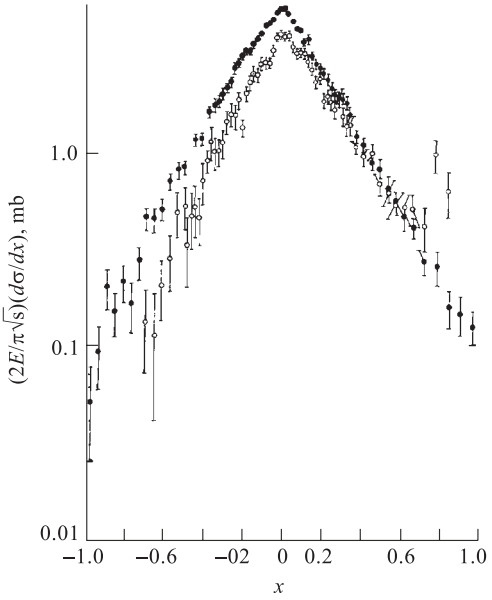

Fig. 6. The x_F distribution of π^+ from $\pi^- p$ collisions: ○ — 5 GeV/c; ● — 40 GeV/c of incident momentum

Table 2. **Threshold values and the values corresponding to the points of maxima of $\xi^\pm$ variables for different intervals of transverse momentum $p_\perp^c$**

Particle type	Interval of $p_\perp^c$, GeV/c	5 GeV/c			40 GeV/c		
		$\lvert\xi_{\rm th}^\pm\rvert = m^c/\sqrt{s}$	$\tilde{\xi}^+$	$\tilde{\xi}^-$	$\lvert\xi_{\rm th}^\pm\rvert = m^c/\sqrt{s}$	$\tilde{\xi}^+$	$\tilde{\xi}^-$
γ	0–0.2	0	0.080	–0.080	0	0.030	–0.030
γ	0.2–0.5	0.060	0.130	–0.170	0.020	0.090	–0.050
π^+	0–0.1	0.040	0.070	–0.070	0.016	0.030	–0.030
π^-	0–0.1	0.040	0.070	–0.070	0.016	0.030	–0.030
π^+	0.1–0.2	0.053	0.090	–0.090	0.020	0.050	–0.030
π^-	0.1–0.2	0.053	0.090	–0.090	0.020	0.050	–0.050
π^+	0.2–0.3	0.076	0.110	–0.110	0.028	0.050	–0.050
π^-	0.2–0.3	0.076	0.110	–0.110	0.028	0.050	–0.050
π^+	0.3–0.4	0.103	0.150	–0.130	0.038	0.070	–0.070
π^-	0.3–0.4	0.103	0.150	–0.150	0.038	0.090	–0.090
π^+	0.4–0.5	0.132	0.170	–0.170	0.048	0.070	–0.070
π^-	0.4–0.5	0.132	0.170	–0.170	0.048	0.110	–0.070
π^+	0.5–1.0	0.162	0.250	–0.230	0.059	0.130	–0.150
π^-	0.5–1.0	0.162	0.290	–0.210	0.059	0.170	–0.130

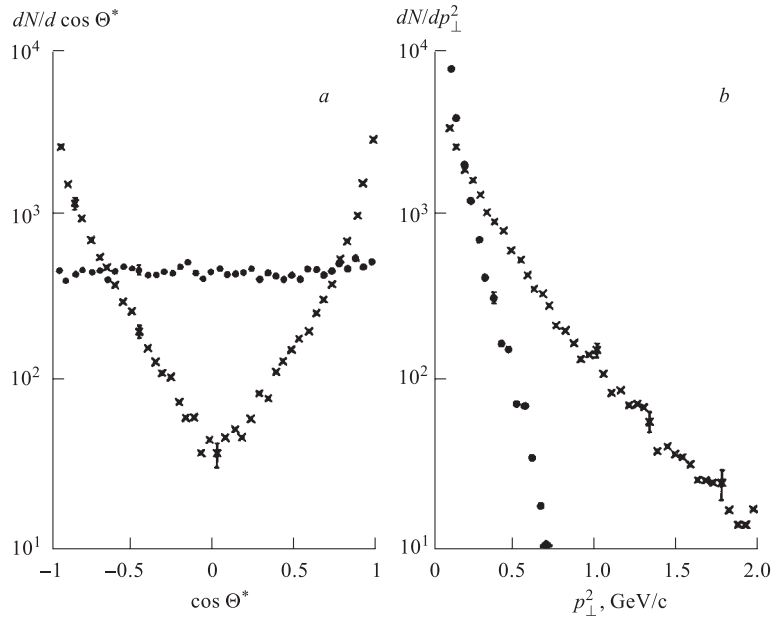

Fig. 7. Angular and $p_\perp^2$ distributions of π^+ mesons from $\pi^- p$ collisions at 40 GeV/c with $\xi^\pm < \tilde{\xi^\pm}$ (•) and $\xi^\pm > \tilde{\xi^\pm}$ (×)

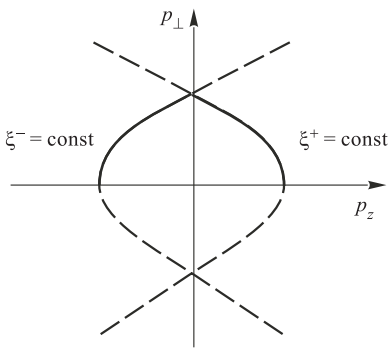

Fig. 8. The schematic view of the surfaces of const $\xi^\pm$

tererstng to note that in the region $|\zeta^\pm| > |\tilde{\zeta}^\pm|$ experimental distributions at these two values of s_1 and s_2 (square of the total energy in the c. m. s.) are almost parallel curves separated from each other to the distance

$$\Delta^\pm = \frac{1}{2} \ln \frac{s_2}{s_1} \tag{23}$$

in the ζ scale. It seems to be interesting to check this regularity at other energies and for other produced particles. It will be worth to investigate this phenomenon in $e^+ - e^-$ annihilation and in nucleus–nucleus collisions.

The almost flat $\cos\Theta$ distribution in the region $|\xi^\pm| < |\tilde{\xi}^\pm|$ allows one to conclude that the thermal equilibrium seems to be reached. In order to check this hypothesis, we have studied the inclusive reaction $\bar{p}p \to \pi^\pm + X$

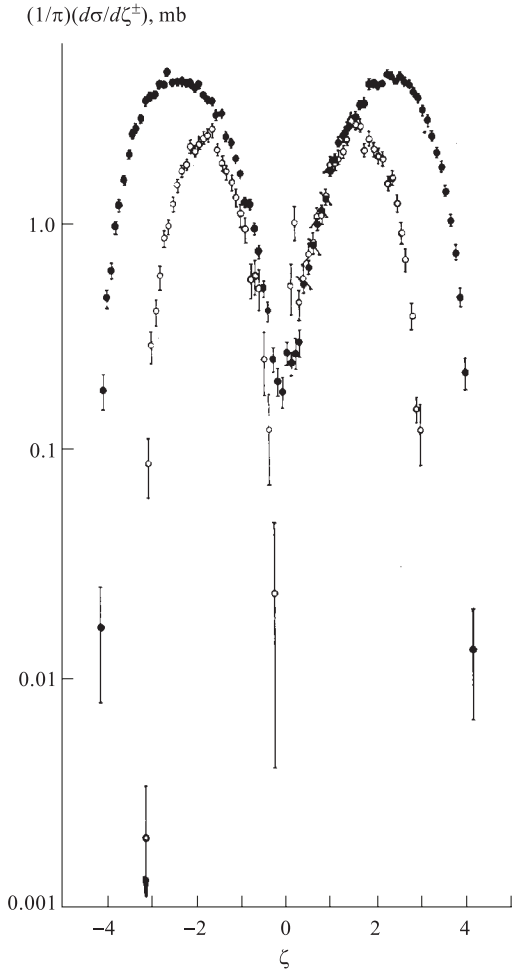

Fig. 9. The $\zeta^{\pm}$ distribution of π^{+} mesons from $\pi^{-}p$ collisions at 5 GeV/c (○) and 40 GeV/c (●) of incident momentum

at 22.4 GeV/c, which has been detected in the two-metre Hydrogen Bubble Chamber of JINR. Details of experiment can be found in Ref. 36. In this case it is sufficient to study the right-hand side hemisphere only, due to the CP symmetry of the reaction.

In Fig. 10 ξ^{+} and ζ^{+} distributions of $\pi^{\pm}$ mesons are shown. In Fig. 11 the angular and $p_{\perp}^{2}$ distributions in two different regions of phase space are given.

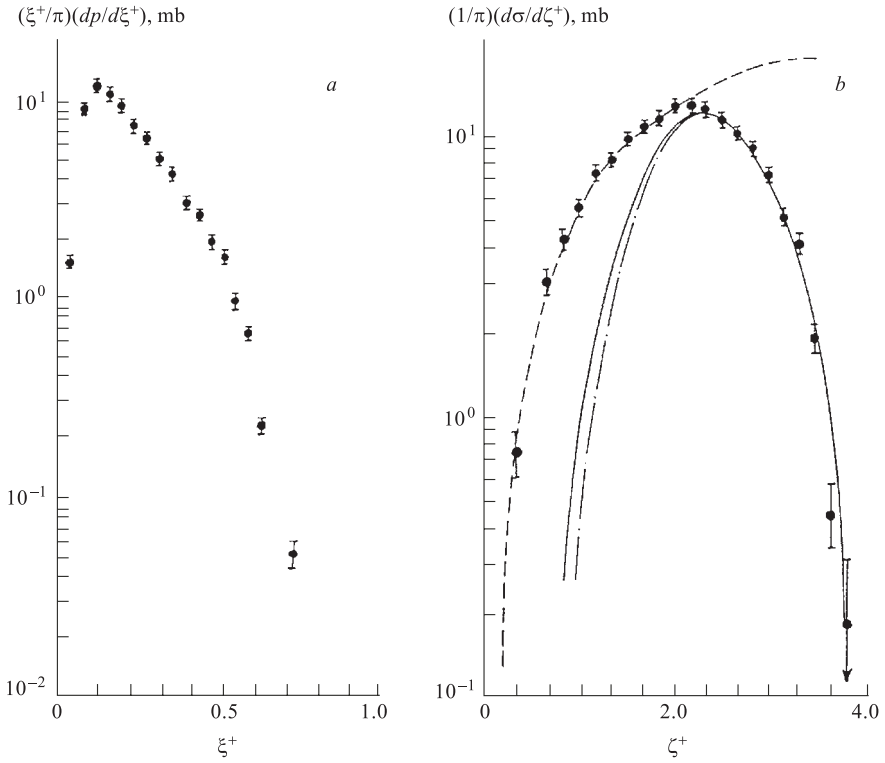

Fig. 10. $(\xi^+/\pi)\,(d\sigma/d\xi^+)$ distribution (*a*) and $(1/\pi)\ (d\sigma/d\zeta^+)$ distribution (*b*) of $\pi^\pm$ mesons in the reaction $\bar{p}p \to \pi^\pm X$ at 22.4 GeV/c. Solid curve — fit of the data in the region $\xi^+ < \tilde{\xi}^+(\zeta^+ > \tilde{\zeta}^+)$ by the Bose–Einstein distribution; dashed-dotted curve — fit of the data in the region $\xi^+ < \tilde{\xi}^+(\zeta^+ > \tilde{\zeta}^+)$ by the Boltzmann distribution; dashed curve — fit of the data in the region $\xi^+ > \tilde{\xi}^+(\zeta^+ < \tilde{\zeta}^+)$ by the formula $(1-\xi^+)^n$

To describe the spectra in the region $\xi^+ < \tilde{\xi}^+(\zeta^+ > \tilde{\zeta}^+)$, the simplest statistical model (see, e. g., [37]) with the Boltzmann $f(E) \sim \mathrm{e}^{-E/T}$ and the Bose–Einstein $f(E) \sim (\mathrm{e}^{E/T}-1)^{-1}$ distributions has been used.

The distributions $(1/\pi)\,(d\sigma/d\zeta^+)$, $d\sigma/dp_T^2$, and $d\sigma/d\cos\Theta$ look in this region as follows:

$$\frac{1}{\pi}\frac{d\sigma}{d\zeta^+} \sim \int\limits_0^{p^2_{T,\max}} Ef(E)dp_T^2, \tag{24}$$

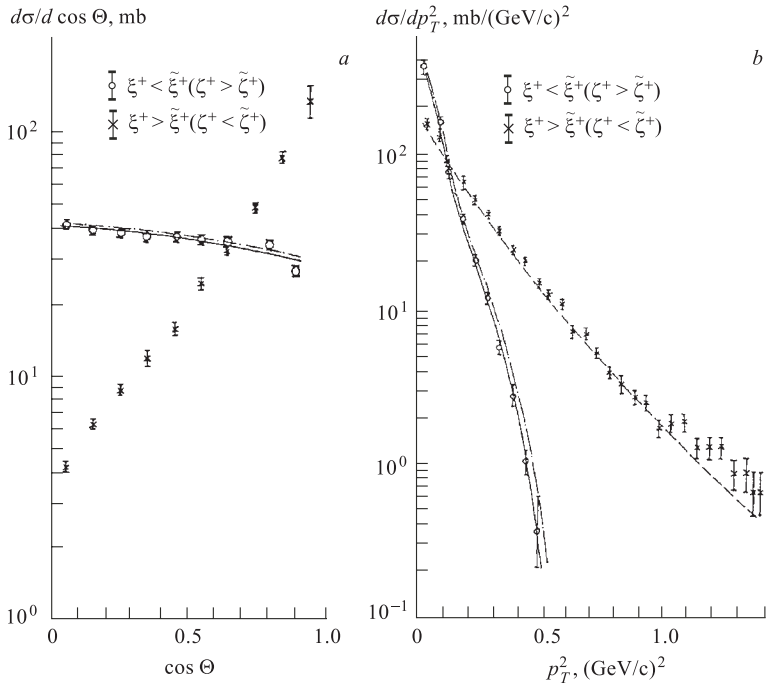

Fig. 11. Angular distribution (*a*) and p_T^2 distribution (*b*) of $\pi^{\pm}$ mesons in the reaction $\bar{p}p \to \pi^{\pm}X$ at 22.4 GeV/c (*a*) and (*b*). Solid curve — fit of the data in the region $\xi^+ < \tilde{\xi}^+(\zeta^+ > \tilde{\zeta}^+)$ by the Bose–Einstein distribution; dashed-dotted curve — fit of the data in the region $\xi^+ < \tilde{\xi}^+(\zeta^+ > \tilde{\zeta}^+)$ by the Boltzmann distribution; dashed curve — fit of the data in the region $\xi^+ > \tilde{\xi}^+(\zeta^+ < \tilde{\zeta}^+)$ by the formula (32)

$$\frac{d\sigma}{dp_T^2} \sim \int_0^{p_{z,\max}} f(E)dp_z, \tag{25}$$

$$\frac{d\sigma}{d\cos\Theta} \sim \int_0^{p_{\max}} f(E)p^2dp, \tag{26}$$

$$E = \sqrt{\mathbf{p}^2 + m_\pi^2}, \quad \mathbf{p}^2 = p_z^2 + p_T^2, \tag{27}$$

where

$$p_{T,\max}^2 = (\xi^+\sqrt{s})^2 - m_\pi^2, \tag{28}$$

$$p_{z,\max} = \frac{p_T^2 + m_\pi^2 - (\tilde{\xi}^+\sqrt{s})^2}{-2\tilde{\xi}^+\sqrt{s}}, \tag{29}$$

$$p_{\max} = \frac{-\tilde{\xi}^+\sqrt{s}\cos\Theta + \sqrt{(\tilde{\xi}^+\sqrt{s})^2 - m_\pi^2\sin^2\Theta}}{\sin^2\Theta}. \tag{30}$$

Table 3. **Results of the fits of** $(1/\pi)(d\sigma/d\zeta^+)$**,** $d\sigma/d\cos\Theta$**, and** $d\sigma/dp_T^2$ **distributions in the region** $\xi^+ < \tilde{\xi}^+(\zeta^+ > \tilde{\zeta}^+)$

	T, GeV	
	Bose–Einstein	Boltzmann
$\frac{1}{\pi}\frac{d\sigma}{d\zeta^+}$	0.134 ± 0.004	0.119 ± 0.003
$\frac{d\sigma}{d\cos\Theta}$	0.091 ± 0.003	0.086 ± 0.003
$\frac{d\sigma}{dp_T^2}$	0.110 ± 0.001	0.105 ± 0.001

The experimental distributions $(1/\pi)(d\sigma/d\zeta^+)$, $d\sigma/dp_T^2$, and $d\sigma/d\cos\Theta$ in the region $\xi^+ < \tilde{\xi}^+(\zeta^+ > \tilde{\zeta}^+)$ have been fitted by Eqs. (24), (25), and (26), respectively. The results of the fit given in Table 3 and Figs. 10, *b*, 11, *a*, 11, *b* show satisfactory agreement with experiment. Thus the spectra of $\pi^\pm$ mesons in the region $\xi^+ < \tilde{\xi}^+(\zeta^+ > \tilde{\zeta}^+)$ are satisfactorily described by the formulae which follow from the statistical model. The same formulae when extrapolated to the region $\xi^+ > \tilde{\xi}^+(\zeta^+ < \tilde{\zeta}^+)$ deviate from the data.

In the region $\xi^+ > \tilde{\xi}^+(\zeta^+ < \tilde{\zeta}^+)$, ζ^+ distribution has been fitted by the formula

$$\frac{1}{\pi}\frac{d\sigma}{d\zeta^+} \sim (1-\xi^+)^n = (1-\mathrm{e}^{-\zeta^+})^n; \tag{31}$$

and the p_T^2 distribution, by the formula

$$\frac{d\sigma}{dp_T^2} \sim \alpha\,\mathrm{e}^{-\beta_1 p_T^2} + (1-\alpha)\,\mathrm{e}^{-\beta_2 p_T^2}. \tag{32}$$

Table 4. **Results of the fits of** $d\sigma/d\zeta^+$ **and** $(1/\pi)\,(d\sigma/dp_T^2)$ **distributions in the region** $\xi^+ > \tilde{\xi}^+(\zeta^+ < \tilde{\zeta}^+)$

	α	β_1, $(\mathrm{GeV/c})^{-2}$	β_2, $(\mathrm{GeV/c})^{-2}$	n
$\frac{1}{\pi}\frac{d\sigma}{d\zeta^+}$	—	—	—	3.7 ± 0.1
$\frac{d\sigma}{dp_T^2}$	0.8 ± 0.03	6.0 ± 0.1	2.8 ± 0.3	—

Thus, the dependence $(1-\xi^+)^n$ is in good agreement with the data in the region $\xi^+ > \xi^+(\zeta^+ < \tilde{\zeta}^+)$ and deviates from them in the region $\xi^+ < \tilde{\xi}^+(\zeta^+ > \tilde{\zeta}^+)$ (see Fig. 10, *b*).

Note that in the region $\xi^+ \to 1$, the parameterization (31) goes over to the well-known quark–parton model parameterization $(1-x)^n$ with $x = x_F = 2p_z/\sqrt{s}$. The results of the fit are given in Table 4 and Figs. 10, *b* and 11, *b*. Since the dependence $(1-x)^n$, which is derived for $x \to 1$, describes the data even in the region $x \to 0$ (where, in general, it must not work), but the dependence (31) deviates from the data in the region of small ξ^+, it seems that the analysis of data in terms of $\xi^\pm$ and $\zeta^\pm$ distributions is more sensitive to the phenomenological models of multibody production at high energies than the analysis in terms of x_F.

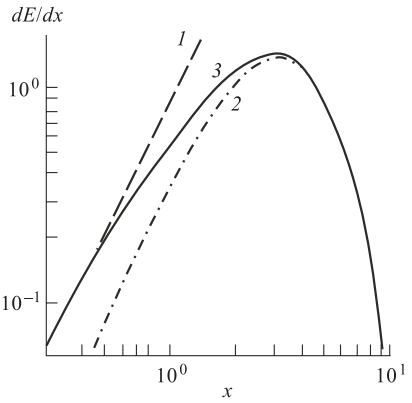

Fig. 12. Black-body radiation intensity as a function of $x = \hbar\omega/kT$: *1* — $dE_\omega \sim x^2 dx$ (Wien); *2* — $dE_\omega \sim x^3 \mathrm{e}^{-x} dx$ (Rayleigh–Jeans); *3* — $dE_\omega \sim x^3(\mathrm{e}^{-x}-1)^{-1} dx$ (Planck)

It is interesting to recall the similar situation in the study of black-body radiation, where the Wien formula describes the low frequency part of the spectrum and does not describe the high frequency part, whereas the situation is reversed in the case of Rayleigh–Jeans formula (see, e. g., [38]). To illustrate this in Fig. 12, the black-body radiation intensity according to the Wien, Rayleigh–Jeans and Planck formulae are plotted against the dimensionless variable $x = \hbar\omega/kT$.

3. NUCLEUS–NUCLEUS COLLISIONS

The study of π^- mesons produced in the relativistic nucleus–nucleus collisions in terms of the light front variables [39–41] has been performed. The choice of the light front variables is due to the fact, that, as one can see from the prevoius sections, these variables seem to be more sensitive to the dynamics of interaction as compared to the well-known Feynman variable x_F and rapidity y. The analysis has been carried out in the nucleus–nucleus centre-of-mass system for π^- mesons from 6147 — He(Li, C), 902 — C–Ne, 6261 — Mg–Mg, 1203 — C–Cu, and 732 — O–Pb collisions [39, 40] obtained on the SKM-200-GIBS facility of JINR and for π^- mesons from 8371 — p–C, 13318 — He–C, 20594 — C–C, and 1989 — C–Ta collisions collected with the two-metre Propane Bubble Chamber (PPK-500) of JINR [41].

Table 5. **Number of events, trigger and the results of the joint fit of the distributions** $(1/\pi)(dN/d\zeta^+)$**,** dN/dp_T^2**,** $dN/d\cos\Theta$ **of** π^- **mesons by Eqs. (24)–(26) in the region** $\zeta^+ > \tilde{\zeta}^+$ **and** $(1/\pi)(dN/d\zeta^+)$ **distributions by Eq. (31) in the region** $\zeta^+ < \tilde{\zeta}^+$

$A_p - A_T$ $T(\Theta_{\rm ch}, \Theta_n)$		Number of events	T, MeV $\zeta^+ > \tilde{\zeta}^+$	n $\zeta^+ < \tilde{\zeta}^+$
He(Li, C)	Exp.	6147	81 ± 2	3.6 ± 0.2
$T(2,0)$	QGSM	15566	84 ± 2	3.5 ± 0.1
C–Ne	Exp.	902	79 ± 3	3.7 ± 0.2
$T(2,0)$	QGSM	3950	82 ± 2	3.4 ± 0.8
Mg–Mg	Exp.	6261	76 ± 2	4.3 ± 0.1
$T(2,2)$	QGSM	6212	77 ± 2	4.2 ± 0.1
C–Cu	Exp.	1203	72 ± 2	3.0 ± 0.1
$T(3,3)$	QGSM	3463	74 ± 2	3.2 ± 0.8
O–Pb	Exp.	732	55 ± 3	2.6 ± 0.1

SKM-GIBS consists of a 2-m streamer chamber, placed in a magnetic field of 0.8 T, and a triggering system. The streamer chamber was exposed to the beam of He, C, O, Ne, and Mg nuclei accelerated in the synchrophasotron up to the energy of 3.7 GeV/nucleon. The thickness of the solid targets in the shape of

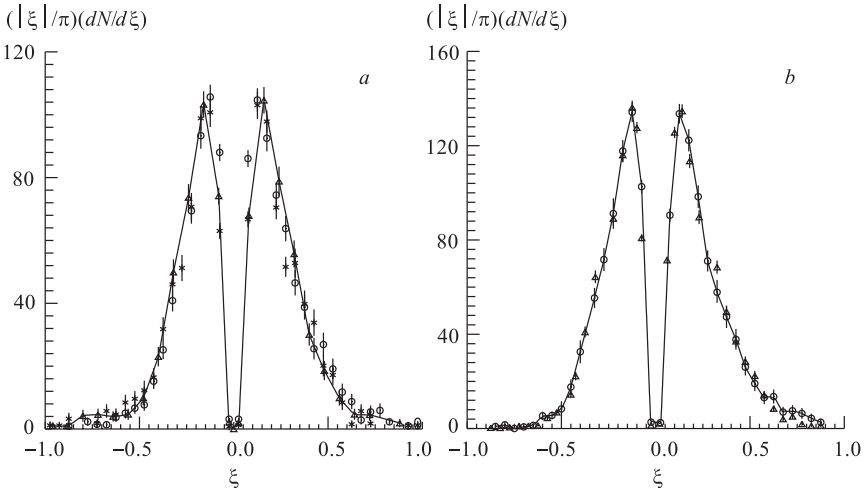

Fig. 13. The $\xi^{\pm}$ distribution of π^- mesons from different interactions: *a*) $*$ — He(Li, C); $\triangle$ — C–Ne; $\circ$ — O–Pb; *b*) from C–Cu interactions: $\circ$ — the experimental data; $\triangle$ — the QGSM data. The curves are the result of polynomial approximation of the experimental data

thin discs was $0.2 \div 0.4$ g/cm^2 (for Li the thickness was 1.59 g/cm^2). Neon gas filling the chamber also served as a nuclear target. The triggering system allowed the selection of «inelastic» and «central» collisions. The «central» trigger was selecting events with no charged projectile spectator fragments (with $P/Z > 3$ GeV/c) within a cone of half-angle $\Theta_{\rm ch}$, $\Theta_n = 2.4^\circ$ or 2.9°. The trigger mode for each exposure is defined as $T(\Theta_{\rm ch}, \Theta_n)$. The number of events for all pairs of nuclei and corresponding trigger modes are listed in Table 5. Due to the small statistics and average multiplicities, the data of He–Li and He–C collisions have been united and thus He(Li, C) represents this sample of the data. In Figs. 13 and 14, the $\xi^{\pm}$ distributions of π^- mesons from He(Li, C), C–Ne, Mg–Mg, C–Cu, and O–Pb interactions are presented. These distributions are similar for all analysed pairs of nuclei. One can see from Figs. 13 and 14 that the principal differences of $\xi^{\pm}$ distributions as compared to the corresponding x_F distributions (Figs. 15 and 16) are the following:

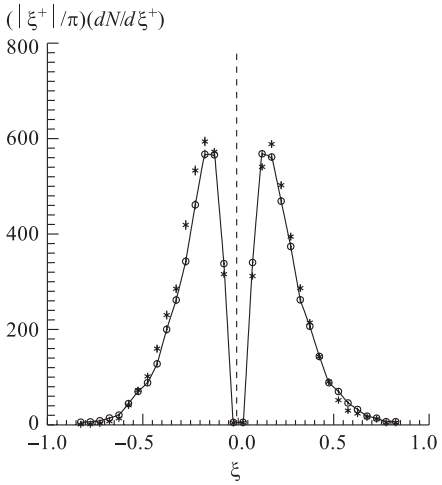

Fig. 14. The $\xi^{\pm}$ distribution of π^- mesons from Mg–Mg interactions: ○ — experimental data; ⋆ — QGSM data; the curve is a result of polynomial approximation of the experimental data

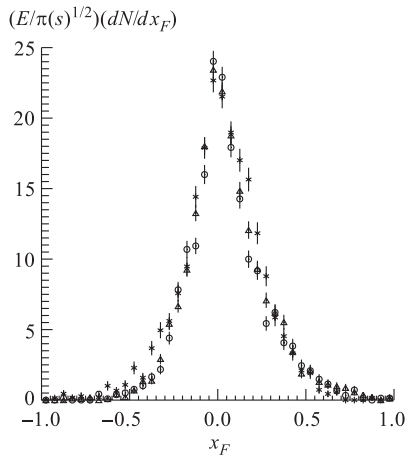

Fig. 15. The x_F distribution of π^- mesons from He(Li, C) (∗), C–Cu (△) and O–Pb (○) interactions

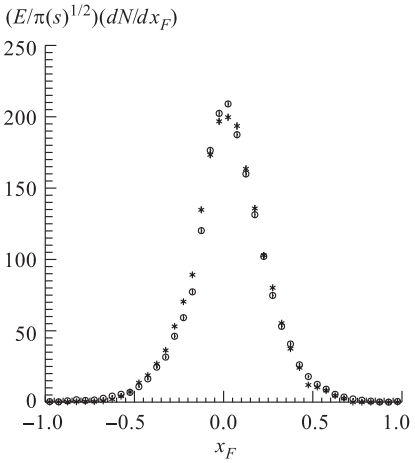

Fig. 16. The x_F distribution of π^- mesons from Mg–Mg interactions: ○ — experimental data; ⋆ — QGSM data

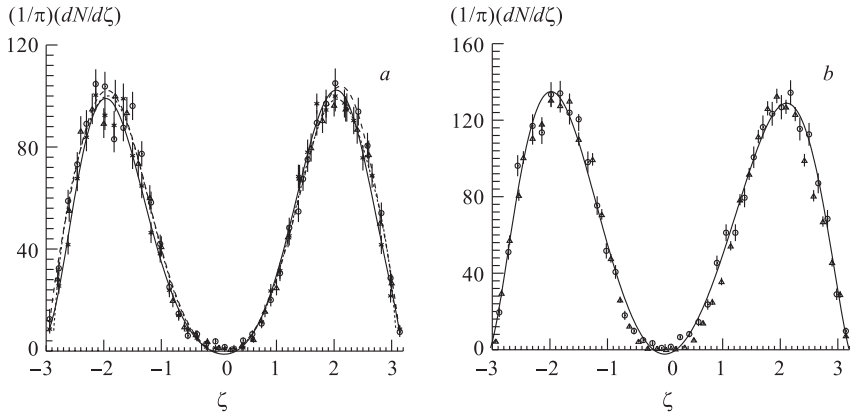

Fig. 17. The $\zeta^{\pm}$ distribution of π^- mesons from different interactions: *a*) $*$ — He(Li, C); $\triangle$ — C–Ne; $\circ$ — O–Pb; *b*) from C–Cu interactions: $\circ$ — the experimental data; $\triangle$ — the QGSM data. The curves are the result of polynomial approximation of the experimental data

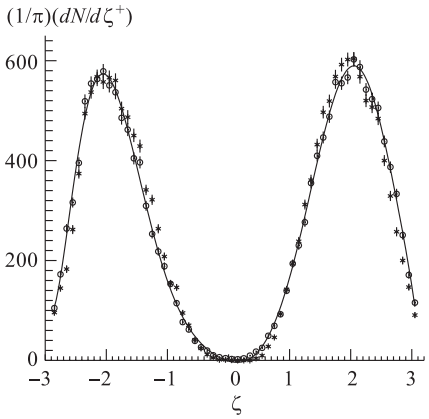

Fig. 18. The $\zeta^{\pm}$ distribution of π^- mesons from Mg–Mg interactions: $\circ$ — experimental data; $\star$ — QGSM data; the curve — result of polinomial approximation of the experimental data

1) existence of some forbidden region around the point $\xi^{\pm} = 0$;

2) existence of maxima at some $\tilde{\xi}^{\pm}$ in the region of relatively small $|\xi^{\pm}|$;

3) existence of limits for $|\xi^{\pm}| \leq m/\sqrt{s})$, similarly to hadron–hadron collisions.

The experimental data for invariant distributions $(1/\pi)(dN/d\zeta^{\pm})$ are shown in Figs. 17 and 18. The curves are the result of the polynomial approximation of the experimental distributions. The maxima at $\tilde{\zeta}^{\pm}$ are also observed in the invariant distributions $(1/\pi)(dN/d\zeta^{\pm})$. However, the region $|\xi^{\pm}| > |\tilde{\xi}^{\pm}|$ goes over to the region $|\zeta^{\pm}| < |\tilde{\zeta}^{\pm}|$ and vice versa (see Eqs. (11) and (12)). The values of maxima are observed at $\tilde{\zeta}^{\pm} = 2.0 \pm 0.1$ for all pairs of nuclei. The $\tilde{\zeta}^{\pm}$ is the function of the energy (see Eqs. (11), (12)) and does not depend on the mass numbers of the projectile (A_P) and target (A_T).

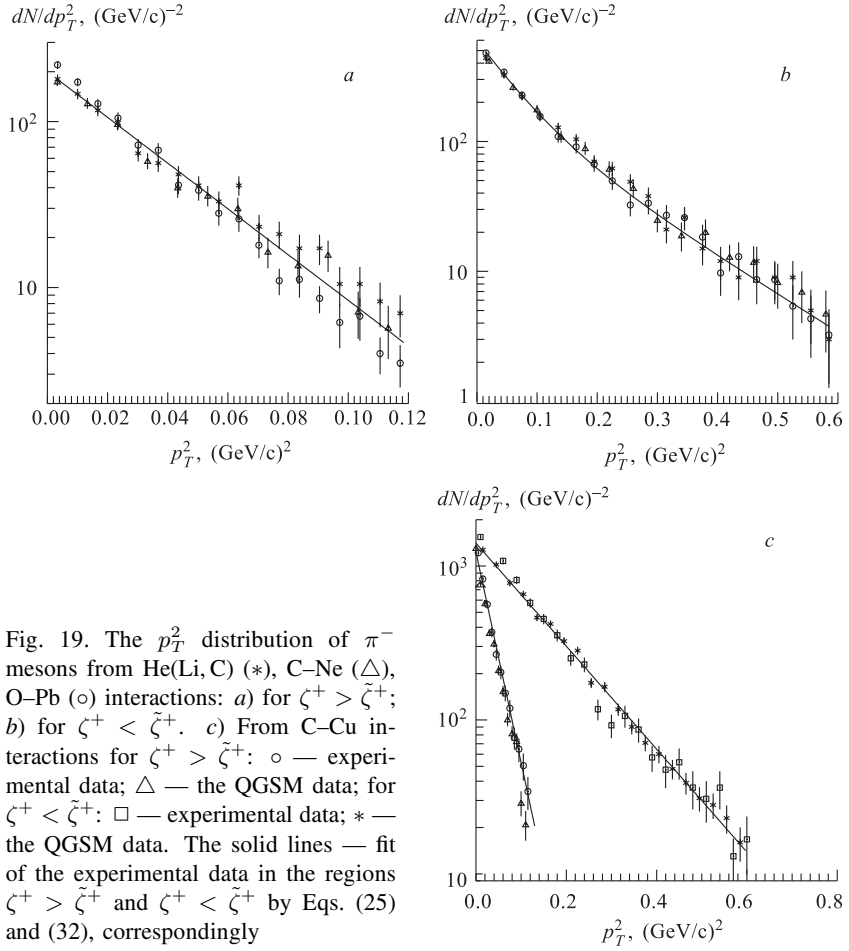

Fig. 19. The p_T^2 distribution of π^- mesons from He(Li, C) ($*$), C–Ne ($\triangle$), O–Pb ($\circ$) interactions: *a*) for $\zeta^+ > \tilde{\zeta}^+$; *b*) for $\zeta^+ < \tilde{\zeta}^+$. *c*) From C–Cu interactions for $\zeta^+ > \tilde{\zeta}^+$: $\circ$ — experimental data; $\triangle$ — the QGSM data; for $\zeta^+ < \tilde{\zeta}^+$: $\square$ — experimental data; $*$ — the QGSM data. The solid lines — fit of the experimental data in the regions $\zeta^+ > \tilde{\zeta}^+$ and $\zeta^+ < \tilde{\zeta}^+$ by Eqs. (25) and (32), correspondingly

In order to study the nature of these maxima, the phase space has been divided into two parts $|\zeta^{\pm}| > |\tilde{\zeta}^{\pm}|$ ($\tilde{\zeta}^+ = 2.0$) and $|\zeta^{\pm}| < |\tilde{\zeta}^{\pm}|$, and the p_T^2 and the angular distributions of π^- mesons in these regions have been studied separately. The numbers of pions in these two regions are approximately equal. For example in C–Cu interactions in the region $|\zeta^{\pm}| > |\tilde{\zeta}^{\pm}|$ the number of pions is equal to -1987; and in $|\zeta^{\pm}| < |\tilde{\zeta}^{\pm}|$, to 2212. In Figs. 19–22 the p_T^2 and the angular distributions of π^- mesons from He(Li, C), C–Ne, Mg–Mg, C–Cu, and O–Pb interactions in different regions of ζ^+ ($\zeta^+ > \tilde{\zeta}^+$ and $\zeta^+ < \tilde{\zeta}^+$) in the forward hemisphere are presented.

One can see from Figs. 19–22 that the p_T^2 and the angular distributions of π^- mesons differ significantly in $\zeta^+ > \tilde{\zeta}^+$ and $\zeta^+ < \tilde{\zeta}^+$ regions. The angular

distribution of pions in the region $\zeta^+ < \tilde{\zeta}^+$ (Figs. 21, *b*, *c* and 22) is sharply anisotropic in contrast to the almost flat distribution in the region $\zeta^+ > \tilde{\zeta}^+$ (Figs. 21, *a*, *c* and 22). The flat behaviour of the angular distribution allows one to think that one observes a partial thermal equilibrium in the region $|\zeta^{\pm}| > |\tilde{\zeta}^{\pm}|$ ($|\xi^{\pm}| < |\tilde{\xi}^{\pm}|$) of phase space. The slopes of p_T^2 distributions differ greatly in different regions of $\zeta^{\pm}$ (Figs. 19 and 20). For example in Mg–Mg interactions: $\langle p_T^2 \rangle = (0.027 \pm 0.002)$ (GeV/c)^2 in the region $\zeta^+ > \tilde{\zeta}^+$; $\langle p_T^2 \rangle = (0.103 \pm 0.009)$ (GeV/c)^2 in the region $\zeta^+ < \tilde{\zeta}^+$.

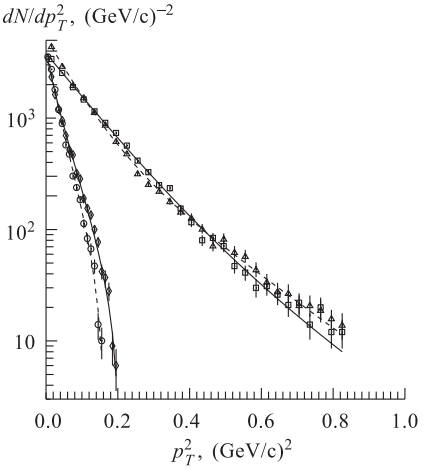

Fig. 20. The p_T^2 distribution of π^- mesons from Mg–Mg interactions: $\circ$ — experimental data for $\zeta^+ > \tilde{\zeta}^+$ ($\tilde{\zeta}^+ = 2.0$); $\diamond$ — the QGSM data for $\zeta^+ > \tilde{\zeta}^+$; $\triangle$ — experimental data for $\zeta^+ < \tilde{\zeta}^+$; $\square$ — the QGSM data for $\zeta^+ < \tilde{\zeta}^+$; dashed lines — fit of the experimental data by the Boltzmann distribution; solid lines — fit of the QGSM data by the Boltzmann distribution

Thus the values of $\tilde{\zeta}^{\pm}$ are the boundaries of the two regions with significantly different characteristics of π^- mesons. The validity of this statement can be seen from the momentum distributions of π^- mesons in the laboratory frame. Figure 23 presents the momentum disribution of pions from C–Cu collisions in the laboratory frame. The shaded area corresponds to the region of $\zeta^+ > \tilde{\zeta}^+$ and the nonshaded one to the region of $\zeta^+ < \tilde{\zeta}^+$. One can see from Fig. 23 that these two regions almost do not overlap in the momentum space unlike to the c. m. s. case (overlap $\sim 45\,\%$). The pions from the region $\zeta^+ > \tilde{\zeta}^+$ have small momentum, approximately up to 0.6 GeV/c as compared to the pions from $\zeta^+ < \tilde{\zeta}^+$ (the momentum of pions ranges from ~ 0.6 to 3 GeV/c). Similar results have been also obtained for the other pairs of nuclei. Figure 24 presents the dependence of $\langle P \rangle_{\rm lab}$ on $\Theta_{\rm lab}$ for all analysed pairs of nuclei (He(Li, C), and C–Ne data are presented with the same symbol because of the similarity of their dependences) in the $\zeta^+ > \tilde{\zeta}^+$ and $\zeta^+ < \tilde{\zeta}^+$ regions. The shapes of these dependences are different in two regions of ζ^+. The curves are the result of polynomial approximation. $\langle P \rangle_{\rm lab}$ decreases and $\langle \Theta \rangle_{\rm lab}$ increases with the increasing of A_P, A_T.

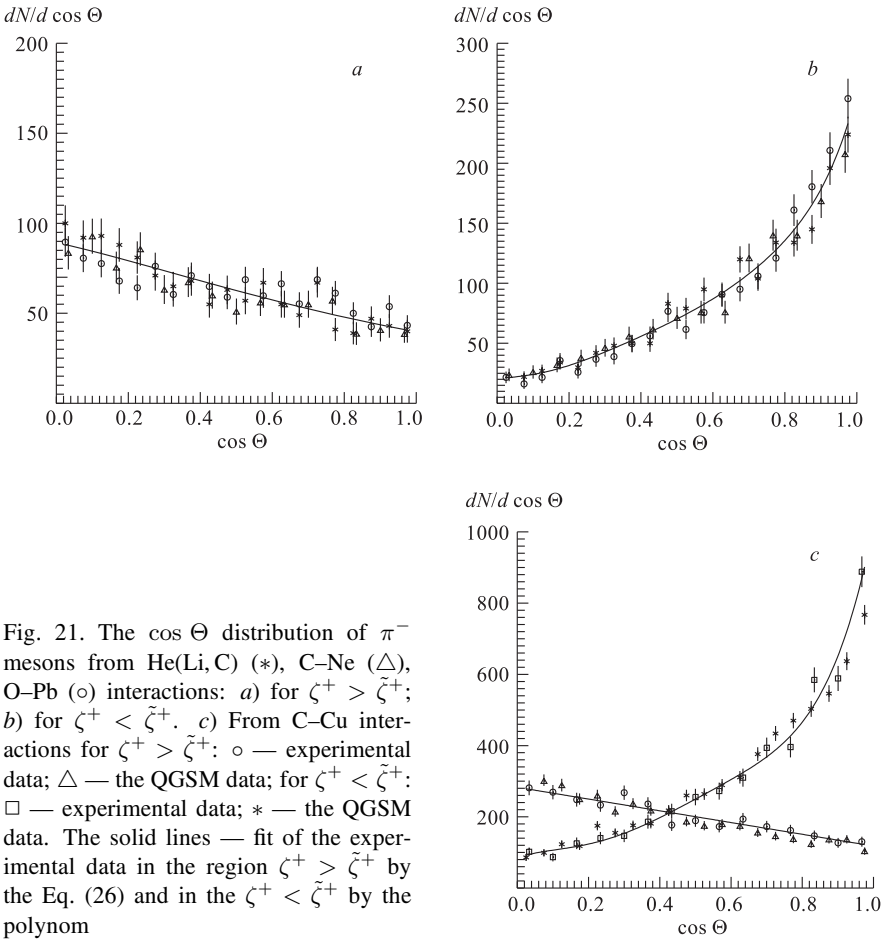

Fig. 21. The $\cos\Theta$ distribution of π^- mesons from He(Li, C) ($*$), C–Ne ($\triangle$), O–Pb ($\circ$) interactions: *a*) for $\zeta^+ > \tilde{\zeta}^+$; *b*) for $\zeta^+ < \tilde{\zeta}^+$. *c*) From C–Cu interactions for $\zeta^+ > \tilde{\zeta}^+$: $\circ$ — experimental data; $\triangle$ — the QGSM data; for $\zeta^+ < \tilde{\zeta}^+$: $\square$ — experimental data; $*$ — the QGSM data. The solid lines — fit of the experimental data in the region $\zeta^+ > \tilde{\zeta}^+$ by the Eq. (26) and in the $\zeta^+ < \tilde{\zeta}^+$ by the polynom

To describe the spectra in the region $\zeta^+ > \tilde{\zeta}^+$, the Boltzmann

$$f(E) \sim \mathrm{e}^{-E/T}$$

distribution has been used.

The distributions $(1/\pi)(dN/d\zeta^+)$, dN/dp_T^2, $dN/d\cos\Theta$ are given by formulae (24)–(27). The experimental distributions in the region $\zeta^+ > \tilde{\zeta}^+$ have been fitted by the expressions (24)–(26), respectively. The results of the joint fit of the distributions $(1/\pi)(dN/d\zeta^+)$, dN/dp_T^2, $dN/d\cos\Theta$ are given in Table 5 and Figs. 19–22. They show a rather good agreement with experiment. In Table 5 the values of the parameter T obtained by fitting the data with Boltzmann distribution

are presented. In order to determine how the characteristics vary, the analysis has been carried out also for $\tilde{\zeta}^+ = 1.9$ and 2.1. The results are similar, but the joint fit of the distributions is better for $\tilde{\zeta}^+ = 2.0$ (presented in figures).

The spectra of π^- mesons in the region $\zeta^+ > \tilde{\zeta}^+$ are satisfactorily described by the formulae which follow from the thermal equilibration. The same formulae

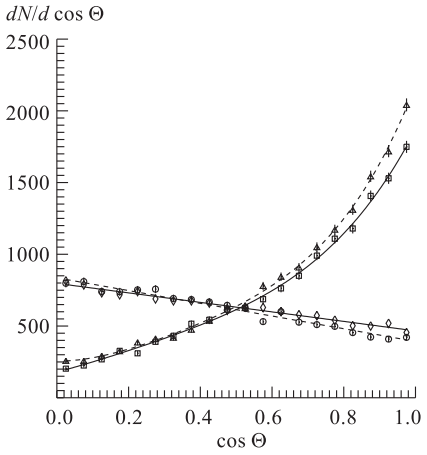

Fig. 22. The $\cos\Theta$ distribution of π^- mesons from Mg–Mg interactions: $\circ$ — experimental data for $\zeta^+ > \tilde{\zeta}^+$ ($\tilde{\zeta}^+ = 2.0$); $\diamond$ — the QGSM data for $\zeta^+ > \tilde{\zeta}^+$; $\triangle$ — experimental data for $\zeta^+ < \tilde{\zeta}^+$; $\square$ — the QGSM data for $\zeta^+ < \tilde{\zeta}^+$; dashed lines — fit of the experimental data; solid lines — fit of the QGSM data

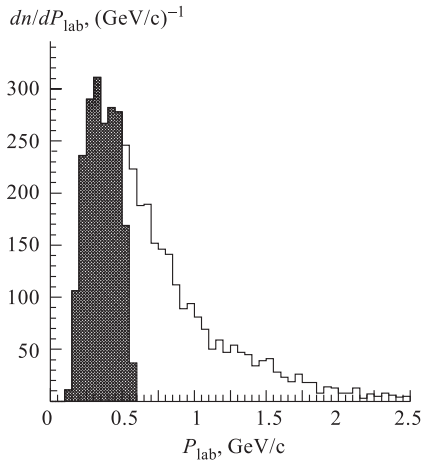

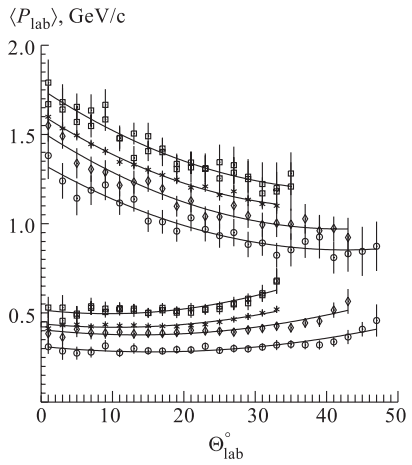

Fig. 23. The momentum distribution of π^- mesons from C–Cu interactions in the laboratory system. The shaded area corresponds to the region of $\zeta^+ > \tilde{\zeta}^+$

Fig. 24. The dependence of $\langle P\rangle_{\rm lab}$ on $\Theta_{\rm lab}$ in the regions $\zeta^+ > \tilde{\zeta}^+$ (bottom data) and $\zeta^+ < \tilde{\zeta}^+$ (top data) for different interactions: $\square$ — He(Li, C) and C–Ne; $\diamond$ — C–Cu; $*$ — Mg–Mg; $\circ$ — O–Pb; the curves — result of polynomial approximation

when extrapolated to the region $\zeta^+ < \tilde{\zeta}^+$ (Figs. 25 and 26) deviate significantly from the data. Therefore in the region $\zeta^+ < \tilde{\zeta}^+$, the p_T^2 distributions have been fitted by formula (32); and the ζ^+ distributions, by formula (31). The dependence (31) $(1 - \mathrm{e}^{-|\zeta^+|})^n$ is in good agreement with experiment in the region $\zeta^+ < \tilde{\zeta}^+$ and deviates from it in the region $\zeta^+ > \tilde{\zeta}^+$ (Figs. 25 and 26). The results of the fit are given in Table 5 and Figs. 19, 20, 25, and 26.

Thus in the $\zeta^\pm$ ($\xi^\pm$) distributions we have singled out points $\tilde{\zeta}^\pm$ ($\tilde{\xi}^\pm$) which separate in the phase space two groups of particles with significantly different characteristics. There are no such points in the x_F and y distributions.

The similar analysis of π^- meson spectra produced in p–C, He–C, C–C, and C–Ta interactions at a momentum of 4.2 GeV/c/nucleon has been carried out in light front variables [41]. The data have been obtained using the 2-m Propane Bubble Chamber of JINR (Dubna), placed in a magnetic field of 1.5 T. The chamber, which housed tantalum targets of thickness about 1mm, was irradiated with protons, deuterons and by relativistic He and C nuclei of incident momenta that varied between 2 and 10 GeV/c per nucleon. From the whole ensemble of

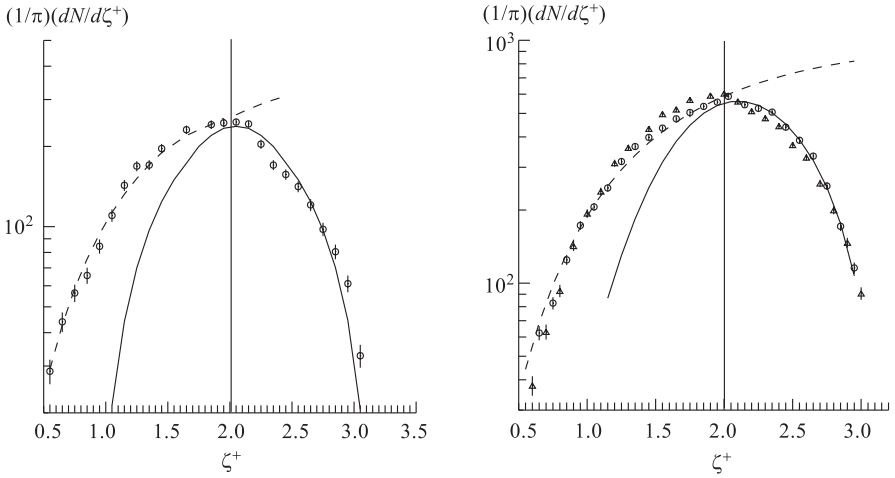

Fig. 25. The $(1/\pi)(dN/d\zeta^+)$ distribution of π^- mesons from C–Cu interactions: $\circ$ — experimental data; the solid line — fit of the experimental data in the region $\zeta^+ > \tilde{\zeta}^+$ by the Eq. (24); the dashed line — fit of the experimental data in the region $\zeta^+ < \tilde{\zeta}^+$ by the Eq. (31)

Fig. 26. The $(1/\pi)(dN/d\zeta^+)$ distribution of π^- mesons from Mg–Mg interactions: $\circ$ — experimental data; $\triangle$ — QGSM data; the solid line — fit of the data in the region $\zeta^+ > \tilde{\zeta}^+$ by the Boltzmann distribution; the dashed line — fit of the data in the region $\zeta^+ < \tilde{\zeta}^+$ by the formula $(1 - \mathrm{e}^{-|\zeta^+|})^n$

Table 6. **Results of the fit of $(1/\pi)(dN/d\zeta^+)$, dN/dp_T^2, $dN/d\cos\Theta$ distributions for π^- mesons by Eqs. (24)–(26) in the region $\zeta^+ > \tilde{\zeta}^+$**

Reaction	$\tilde{\zeta}^{\pm}$	T, MeV		
		$(1/\pi)(dN/d\zeta^+)$	$dN/d\cos\Theta$	dN/dp_T^2
$pC \to \pi^- + X$	2.0	107 ± 15	89 ± 20	75 ± 7
$HeC \to \pi^- + X$	1.8	100 ± 4	99 ± 10	87 ± 3
$CC \to \pi^- + X$	1.9	93 ± 3	60 ± 4	72 ± 2
$CTa \to \pi^- + X$	2.0	71 ± 5	68 ± 10	64 ± 4

collisions of C nuclei in Propane Chamber, inelastic C–C collisions have been selected. The points have been singled out $\tilde{\zeta}^{\pm} : \tilde{\zeta}^{\pm} = 2.0$ for p–C, $\tilde{\zeta}^{\pm} = 1.8$ — He–C, $\tilde{\zeta}^{\pm} = 1.9$ — C–C, and $\tilde{\zeta}^{\pm} = 2.0$ — C–Ta. The spectra of pions have been described with the same formulae, as for SKM-200-GIBS data, and the parameters T ($\zeta^+ > \tilde{\zeta}^+$) and n ($\zeta^+ < \tilde{\zeta}^+$) have been extracted. The results of fits are presented in Tables 6 and 7. One can see (Tables 5–7) that the results of SKM-200-GIBS and of 2-m Propane Bubble Chamber Collaboration (PPK-500) agree quite well. The angular and transverse momentum distributions of π^- mesons in various regions of variables $\xi^{\pm}$ and $\zeta^{\pm}$ in p–C, He–C, C–C, and C–Ta collisions show the characteristics [41] similar to those from He(Li, C), C–Ne, Mg–Mg, C–Cu, and O–Pb collisions of SKM-200-GIBS experiment.

The Quark Gluon String Model was used for the comparison with experimental data of SKM-200-GIBS. He(Li, C), C–Ne, Mg–Mg, C–Cu, and O–Pb interactions have been generated using Monte-Carlo generator COLLI, based on the QGSM. The events have been traced through the detector and trigger filter. The events have been generated for not fixed impact parameter $\tilde{b}$. From the impact parameter distribution the mean value of $\langle b \rangle$ has been obtained. For the obtained value of $\langle b \rangle$, total samples of A_P–A_T events have been generated. The numbers

Table 7. **Results of the fit of $(1/\pi)(dN/d\zeta^+)$, dN/dp_T^2 distributions for π^- mesons by Eqs. (31) and (32) in the region $\zeta^+ < \tilde{\zeta}^+$**

Reaction	dN/dp_T^2			$(1/\pi)(dN/d\zeta^+)$
	α	β_1, $(\text{GeV/c})^{-2}$	β_2, $(\text{GeV/c})^{-2}$	n
$pC \to \pi^- + X$	0.9 ± 0.1	11.3 ± 2.4	3.0 ± 1.5	3.8 ± 0.2
$HeC \to \pi^- + X$	0.9 ± 0.1	7.8 ± 1.1	0	3.8 ± 0.2
$CC \to \pi^- + X$	0.66 ± 0.04	24.0 ± 3.1	6.7 ± 0.4	3.8 ± 0.2
$CTa \to \pi^- + X$	0.8 ± 0.3	11.9 ± 3.0	4.9 ± 3.0	4.4 ± 0.3

of generated events for all analysed pairs of nuclei are listed in Table 5. In SKM-200-GIBS experiment the following values of b are most probable: $b = 1.55$ fm for He(Li, C); $b = 2.20$ fm for C–Ne; $b = 1.34$ fm for Mg–Mg; $b = 2.75$ fm for C–Cu; $b = 3.75$ fm for O–Pb.

The experimental results have been compared with the predictions of the QGSM for the above-mentioned values of b, and satisfactory agreement between the experimental data and the model has been found. In Figs. 13, *b*, 14, 17, *b*, and 18, the $\xi^{\pm}$ and $\zeta^{\pm}$ distributions of π^- mesons from the QGSM calculations are presented together with the experimental ones for C–Cu and Mg–Mg interactions. One can see that the QGSM well reproduces these distributions. The similar results have been obtained for all analysed pairs of nuclei. The QGSM also reproduces the p_T^2 and $\cos\Theta$ distributions (Figs. 19, *c*, 20, 21, *c*, and 22). The QGSM data show the similar characteristics in different regions of ζ as experimental ones: sharply anisotropic angular distributions in the region $\zeta^+ < \tilde{\zeta}^+$ and the almost flat distribution in the region $\zeta^+ > \tilde{\zeta}^+$; the slopes of p_T^2 distributions differ greatly in different regions of ζ^+. The average values of $\langle p_T^2 \rangle$ in these two regions also differ: for example, for Mg–Mg, $\langle p_T^2 \rangle = (0.029 \pm 0.003)$ (GeV/c)^2 in the region $\zeta^+ > \tilde{\zeta}^+$; $\langle p_T^2 \rangle = (0.109 \pm 0.009)$ (GeV/c)^2 in the region $\zeta^+ < \tilde{\zeta}^+$. The average values of $\langle p_T^2 \rangle$ in different regions of ζ from the experimental and QGSM data agree respectively; the momentum distributions of pions in the laboratory frame in different regions of ζ^+ have also different shape of spectra as experimental ones (Fig. 23). Momentum distributions of QGSM data reproduce the corresponding experimental spectra in both regions of ζ^+. The distributions obtained by the QGSM in the region $\zeta^+ > \tilde{\zeta}^+$ have been fitted by the expressions (24)–(26). The results of the fit are given in Table 5 and Figs. 19, *c*, 20, 21, *c* and 22. In the region $\zeta^+ < \tilde{\zeta}^+$, the p_T^2 and the ζ^+ distributions have been fitted by the formulae (32) and (31), respectively. The results of the fit are given in Table 5 and Figs. 19, *c*, 20, 25 and 26. One can see from Table 5 that the values of the T extracted from the experimental and QGSM data coincide within the errors. The QGSM does not reproduce satisfactorily the O–Pb data. This may be caused by the fact, that QGSM simplifies the nuclear effects, which are more pronounced for heavy nuclei. In Ref. 42, it has been indicated that the model can be improved by including higher mass baryon resonances and taking into account a possible increase of the pion absorption cross section, $\sigma_{\Delta\Delta \to NN}$ in dense baryon medium, in comparison with the cross section, obtained from the detailed balance relation.

In Fig. 27, the dependence of the parameter T from Tables 5 and 6 on $(A_P \cdot A_T)^{1/2}$, obtained from the experimental and QGSM data of SKM-200-GIBS and experimental results of PPK-500, is presented. One can see that T decreases linearly with the increasing $(A_P \cdot A_T)^{1/2}$, i. e., with the increasing number of participating nucleons. Similar behaviour is predicted by the QGSM.

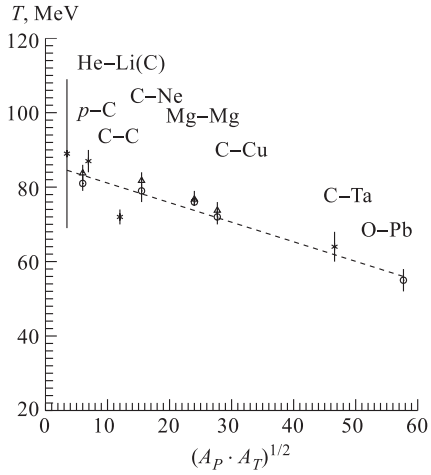

Fig. 27. The dependence of the parameter T on $(A_P \cdot A_T)^{1/2}$ for He(Li, C), C–Ne, Mg–Mg, C–Cu, and O–Pb [38, 39]: $\circ$ — the experimental data; $\triangle$ — the QGSM data; for p–C, He–C, C–C, and C–Ta [40]: $*$ — the experimental data. The dashed line is a result of linear approximation

In Ref. 43, the temperatures of pions in He–Li, He–C, C–Ne, Mg–Mg, C–Cu, and O–Pb interactions were obtained be means of inclusive kinetic energy and transverse momentum spectra in central rapidity interval (0.5–2.1 for light nuclei and 0.1–1.8 for heavy ones), which corresponds to the pionization region and with the c. m. s. angles $90 \pm 10^\circ$. The pion spectra for He–Li, He–C, and C–Ne have been fitted by one exponent; and for Mg–Mg, C–Cu, and O–Pb, by a sum of two exponents, or two temperatures T_1 and T_2 (describing the low and high momentum part of the spectrum). The temperatures extracted by the light front analysis for light pairs of nuclei are less about (15–20) % as compared to those obtained in Ref. 43. For heavy pairs of nuclei, the temperatures are more close to the low temperature T_1. It seems obvious that the thermal equilibrium region corresponds to lower momenta. It should be mentioned that the extraction procedures of T in the light-front variables and in Ref. 43 are quite different and it seems, that different regions of phase space are seperated by these methods.

The temperatures of pions have been extracted in the GSI experiments (FOPI, KAON and TAPS Collaborations, see, e. g., [44–46]). The T in the GSI experiments have been obtained in the same manner as in Ref. 43. FOPI Collaboration [44, 46] has obtained that the π^- spectra from Ni–Ni collisions require the sum of two exponential functions with independent yields, and slope parameters T_l and T_h describe mostly the low and the high momentum parts of the spectrum, respectively: at $E = 1.06$ GeV/nucleon $T_l = (55 \pm 3)$ MeV, $T_h = (93 \pm 5)$ MeV; at $E = 1.45$ GeV/nucleon $T_l = (56 \pm 3)$ MeV, $T_h = (100 \pm 5)$ MeV; at $E = 1.93$ GeV/nucleon $T_l = (61 \pm 3)$ MeV, $T_h = (115 \pm 6)$ MeV. The FRS Collaboration has found that the T for π^- mesons in Ne–NaF collisions vary from (78 ± 2) MeV to (96 ± 3) MeV for projectile energies from 1.34 to 1.94 GeV/nucleon.

TAPS Collaboration has found for π^0 mesons $T = (83 \pm 3)$ MeV in C–C interactions at incident energy of $E = 2$ GeV/nucleon; $T = (70 \pm 1)$ MeV in Ar–Ca interactions at incident energy of $E = 1.5$ GeV/nucleon; KAON Collaboration

has found a value of T for π^+ mesons ranging from (71 ± 3) MeV (at energy $E =$ 1 GeV/nucleon) to (95 ± 3) MeV (at energy $E = 1.8$ GeV/nucleon). The numerical values of the parameter T for pions in Au–Au collisions at 1.0 GeV/nucleon (FOPI) and our values for the heaviest colliding pair are close to each other.

CONCLUSION

A remark on the nature of maxima in $\zeta^{\pm}$ distributions is in order. The ALEPH Collaboration observed the maxima in the ξ distributions ($\xi = -\ln p/p_{\max}$) [47] of secondary hadrons in e^+e^- collisions, which coincide to high precision with predictions of the perturbative QCD (see, e. g., [48, 49]). The accuracy of coincidence increases when next-to-leading order corrections are taken into account. So the shapes of ξ distributions are related to the details of the underlying dynamics. Similarly, it seems that the maxima in $\zeta^{\pm}$ distributions reflect the dynamics of the processes considered. In particular, secondary pions with $|\xi^{\pm}| < |\tilde{\xi}^{\pm}|$ have almost flat angular distribution in the centre-of-mass frame, whereas pions with $|\xi^{\pm}| > |\tilde{\xi}^{\pm}|$ are produced sharply anisotropically. So the phase space of secondary pions is divided into two parts with significantly different characteristics in a unique way. Separation points are points of maxima in corresponding $\xi^{\pm}(\zeta^{\pm})$ spectra (or corresponding paraboloids in the phase space). Thus one can say that the problem of separation of «pionization» and fragmentation components seems to be solved in a unique way. An application of the method proposed to a wide class of hadronic and nucleus–nucleus reactions and e^+e^- annihilation into hadrons seems to be of great interest.

As is mentioned in the Introduction, light front variables define the so-called horospherical coordinate system in the Lobachevsky space. It seems to be interesting to use other coordinate systems on the mass shell hyperboloid (see, e. g., [10]) for the analysis of inclusive spectra.

In conclusion, we think that the use of light front variables can help to distinguish in between different dynamical contributions, or test basic principles in other types of analysis, such as two-particle correlations, HBT-interferometry [50, 51] and transverse flow studies [52].

Acknowledgements. The authors would like to thank the staffs of the 1-m Propane Bubble Chamber, 2-m Propane Bubble Chamber, 2-m Hydrogen Bubble Chamber and SKM-200-GIBS Collaborations of JINR for helping in obtaining the data, fruitful collaboration and many valuable discussions. One of the authors (V. G.) expresses his deep gratitude to V. Kadyshevsky and P. Bogolubov for the warm hospitality at the Laboratory of Theoretical Physics of JINR. Many colleagues from the High Energy Physics Institute of Tbilisi State University contributed to these investigations. The investigations for hadron–hadron collisions have been begun under the leadership of Prof. N. Amaglobeli. The authors

are very indepted to Prof. N. Amaglobeli and express him their deep gratitude. Special thanks are due L. Abesalashvili, B. Chiladze, N. Koutsidi, G. Kuratashvili, R. Kvatadze, Sh. Shoshiashvili, and T. Topuria for helpful collaboration.

REFERENCES

1. *Logunov A. A., Mestvirishvili M. A., Nguen van Hieu* // Phys. Lett. B. 1967. V. 25. P. 611.
2. *Benecke J. et al.* // Phys. Rev. 1969. V. 188. P. 2159.
3. *Feynman R.* // Phys. Rev. Lett. 1969. V. 23. P. 415.
4. *Matveev V. A., Muradyan R. M., Tavkhelidze A. N.* // Lett. Nuovo Cim. 1972. V. 5. P. 907.
5. *Baldin A. M.* // Nucl. Phys. A. 1985. V. 447. P. 203.
6. *Baldin A. M.* // Phys. of Atom. Nucl. 1993. V. 56. P. 385.
7. *Baldin A. M., Didenko L. A.* // Fortsch. der Phys. 1994. V. 38. P. 261.
8. *Abesalashvili L. N. et al.* // JETP Lett. 1978. V. 28. P. 174;
   Abesalashvili L. N. et al. // Proc. of the IV European Antiproton Symp., Strasbourg, 1978;
   Abesalashvili L. N. et al. // Sov. J. Nucl. Phys. 1979. V. 30. P. 156;
   Amaglobeli N. et al. // Eur. Phys. J. C. 1999. V. 8. P. 603.
9. *Dirac P.* // Rev. Mod. Phys. 1949. V. 21. P. 392.
10. *Vilenkin N., Smorodinsky A.* // JETP. 1964. V. 46. P. 1793.
11. *Garsevanishvili V. R. et al.* // Sov. J. Theor. Math. Phys. 1971. V. 7. P. 203.
12. *Leutwyler H.* // Nucl. Phys. B. 1974. V. 76. P. 413.
13. *Garsevanishvili V. R. et al.* // Sov. J. Theor. Math. Phys. 1975. V. 23. P. 310.
14. *Garsevanishvili V. R., Matveev V. A.* // Ibid. V. 24. P. 3.
15. *Garsevanishvili V. R.* // Proc. of the XIII Intern. Winter School of Theor. Phys., Karpacz, Poland, Feb. 1976. Wroclaw, 1976. P. 315.
16. *Sivers D., Brodsky S., Blankenbecler R.* // Phys. Rep. 1976. V. 23. P. 1.
17. *Schmidt I., Blankenbecler R.* // Phys. Rev. D. 1977. V. 15. P. 3321.
18. *Leutwyler H., Stern J.* // Ann. of Phys. (N. Y.). 1978. V. 112. P. 94.
19. *Bakker B. I., Kondratyuk L. A., Terentyev M. V.* // Nucl. Phys. B. 1979. V. 158. P. 497.
20. *Karmanov V. A.* // Part. and Nucl. 1988. V. 19. P. 525.
21. *Kulshreshtha D. S., Mitra A. N.* // Phys. Rev. D. 1988. V. 37. P. 1268.
22. *Garsevanishvili V. R., Menteshashvili Z. R.* Relativistic Nuclear Physics in the Light Front Formalism. N. Y.: Nova Science Publishers, 1993.
23. *Brodsky S. J. et al.* // Particle World. 1993. V. 3. P. 109.
24. *Desplanques B.* // Nucl. Phys. A. 1995. V. 589. P. 697.
25. *Karmanov V. A., Mathiot J.-F.* // Nucl. Phys. A. 1996. V. 602. P. 388.
26. *Carbonell J. et al.* // Phys. Rep. 1998. V. 300. P. 215; nucl-th/9804029.
27. *Aladashvili B. S. et al. (Dubna–Košice–Moscow–Strasbourg–Tbilisi–Warsaw Collab.)* // Sov. J. Nucl. Phys. 1981. V. 34. P. 591.
28. *Azhgirey L. S. et al.* // Phys. Lett. B. 1996. V. 387. P. 37.

29. *Wilson K. G. et al.* // Phys. Rev. D. 1994. V. 49. P. 6720;
Brisudova M. M., Perry R. J., Wilson K. G. // Phys. Rev. Lett. 1997. V. 78. P. 1227.

30. *Kadyshevsky V. G., Mateev M. D., Mir-Kasimov R. M.* // Proc. of the Intern. Seminar on Deep Inelastic and Inclusive Processes, Sukhumi, 1975. M., 1977. P. 221.

31. *Donkov A. D. et al.* // Proc. of V. A. Steklov Mathem. Institute. M., 1975. V. CXXXVI. P. 85.

32. *Belonogov A. V. et al.* // Nucl. Instr. Meth. 1969. V. 20. P. 114;
Glagolev V. V. et al. JINR Commun. 1-4847. Dubna, 1969.

33. *Balandin M. P. et al.* // Nucl. Instr. Meth. 1969. V. 20. P. 110;
Abdurakhimov A. U. et al. JINR Commun. P1-6326. Dubna, 1972.

34. *Bogomolov A. V. et al.* // Nucl. Instr. Meth. 1964. V. 1. P. 61.

35. *Abesalashvili L. N. et al.* // JETP Lett. 1979. V. 30. P. 448.

36. *Boos E. G. et al.* // Nucl. Phys. B. 1980. V. 147. P. 45.

37. *Feinberg E. L.* // UFN. 1971. V. 164. P. 539.

38. *Landau L. D., Lifshitz E. M.* Statistical Physics. M.: Nauka, 1976.

39. *Anikina M. X. et al.* // Nucl. Phys. A. 1998. V. 640. P. 117.

40. *Anikina M. X. et al.* // Eur. Phys. J. A. 2000. V. 7. P. 139.

41. *Akhobadze L. et al.* // Phys. of Atom. Nucl. 2000. V. 63. P. 1670.

42. *Bravina L. et al.* // Nucl. Phys. A. 1994. V. 566. P. 376.

43. *Anikina M. X. et al.* // Z. Phys. C. 1992. V. 54. P. 179.

44. *Hong B. et al.* // Phys. Rev. C. 1998. V. 57. P. 244.

45. *Gilg A. et al.* GSI Scientific Report 96-1. Darmstadt, 1996. P. 52;
Pfeiffer M. et al. GSI Scientific Report 93-1. Darmstadt, 1993. P. 58;
Schwalb O. et al. Ibid. P. 62;
Appenheimer M. et al. GSI Scientific Report 97-1. Darmstadt, 1997. P. 58;
Müntz C. et al. GSI Scientific Report 95-1. Darmstadt, 1995. P. 77.

46. *Herrmann N.* // Nucl. Phys. A. 1996. V. 610. P. 49c.

47. *Ajaltouni Z. et al. (ALEPH Collab.)* CERN/PPE 96-186; Phys. Rep. 1998. V. 294. P. 1.

48. *Fong C.P., Webber B. R.* // Phys. Lett. B. 1989. V. 229. P. 289.

49. *Dokshitzer Yu. L. et al.* Basics of Perturbative QCD. Gif-sur-Yvette: Editions Frontieres, 1991.

50. *Hanbury-Brown R., Twiss R.* // Phil. Mag. 1954. V. 45. P. 663.

51. *Kopylov G. I., Podgoretsky M. I.* // Sov. J. Nucl. Phys. 1974. V. 19. P. 215.

52. *Danielewicz P., Odyniec G.* // Phys. Lett. B. 1985. V. 157. P. 146.